https://doi.org/10.1016/j.buildenv.2021.108413

Cao, Q., Liu, M., Li, X., Lin, C.-H., Wei, D., Ji, S., Zhang, T., and Chen, Q. 2022. "Influencing factors in the simulation of airflow and particle transportation in aircraft cabins by CFD," *Building and Environment,* 207: 108413

Influencing Factors in the Simulation of Airflow and Particle Transportation in Aircraft Cabins by CFD

Qing Cao[a], Mingxin Liu[b], Xingyang Li[b], Chao-Hsin Lin[c], Daniel Wei[d], Shengcheng Ji[e], Tengfei (Tim) Zhang[a,b], and Qingyan Chen[f*]

[a]*School of Civil Engineering, Dalian University of Technology (DUT), Dalian, 116024, China*
[b]*Tianjin Key Laboratory of Indoor Air Environmental Quality Control, School of Environmental Science and Engineering, Tianjin University, Tianjin, 300072, China*
[c]*Environmental Control Systems, Boeing Commercial Airplanes, Everett, WA, 98203, USA*
[d]*Boeing Research & Technology, Beijing, 100027, China*
[e]*Beijing Aeronautical Science & Technology Research Institute of COMAC, Beijing, China*
[f]*Department of Building Environment and Energy Engineering, The Hong Kong Polytechnic University, Kowloon, Hong Kong*

[*]*Corresponding email: qingyan.chen@polyu.edu.hk*

Highlights

- ✧ Evaluation of various factors in the accuracy of CFD simulations
- ✧ Factors include ventilation system, turbulence model, particle simulation method, geometric model, and boundary conditions
- ✧ Comparison of CFD results with experimental data from the literature

Keywords: *CFD, particle transport, mixing ventilation, displacement ventilation, airliner cabin, validation*

ABSTRACT

To control the transport of particles such as the SARS-CoV-2 virus in airliner cabins, which is a significant concern for the flying public, effective ventilation systems are essential. Validated computational fluid dynamics (CFD) models are frequently and effectively used to investigate air distribution and contaminant transportation. The complex geometry and airflow characteristics in airliner cabins pose a challenge to numerical CFD validation. The objective of this investigation was to identify accurate and affordable validation processes for studying the airflow field and particulate contaminant distribution in airliner cabins during the design process for different ventilation systems. This study quantitatively evaluated the effects of ventilation system, turbulence model, particle simulation method, geometry simplification, and boundary condition assignment on airflow and particulate distributions in airliner cabins with either a mixing ventilation (MV) system or a displacement ventilation (DV) system calculated by CFD. The results showed that among four turbulence models, the standard k-ε, RNG k-ε, realizable k-ε and SST k-ω models, the prediction by the realizable k-ε model agreed most closely with the experimental data. Meanwhile, the steady Eulerian method provided a reasonable prediction of the particle concentration field with low computing cost. The computational domain should be simplified differently for the DV system and the MV system with consideration of the simulation accuracy and computing cost. For more accurate modeling results, the boundary conditions should be assigned in greater detail, taking into account the uniformity on the boundary.

1. Introduction

The COVID-19 pandemic has focused significant public attention on the cabin environment in commercial airplanes [1,2]. The air distribution in an airplane plays a pivotal role in the creation of a clean, healthy, and comfortable cabin environment [3,4]. Current airplanes use a mixing ventilation (MV) system to obtain a uniform air distribution. This system supplies clean air at ceiling level and extracts contaminated air at floor level [5]. However, several previous studies found that the MV system was not efficient in controlling contaminant transmission [6-8]. To improve the cabin air quality, recently increasing attention by researchers has been paid to the development of a displacement ventilation (DV) system that supplies conditioned air at floor level at a low velocity and extracts contaminated air at ceiling level. The control of COVID-19 requires careful investigation of the air and contaminant distributions.

To study the airflow and contaminant distributions in an airplane cabin under different ventilation systems, either experimental measurements or computational fluid dynamics (CFD) simulations are commonly used [9]. Compared with experimental methods, CFD modeling is more efficient, and it can be used to analyze multiple cases at low cost [10]. However, it is challenging to accurately simulate airflow and contaminant transmission in an airplane cabin by CFD because of the complex geometry and flow pattern and the approximations used in the modeling method [11]. Previous studies reported discrepancies between the numerical results and experimental data for airflow and contaminant distributions in airplane cabins [12]. It is essential to validate CFD results if this modeling approach is used for airplane studies.

Numerous studies [11-24] have validated CFD results for the distributions of air velocity, air temperature, and gaseous and particulate pollutant concentration in aircraft cabins under mixing ventilation. However, few studies have addressed displacement ventilation [25-27]. Since the flow characteristics in a cabin are different under different ventilation systems, the modeling strategies may not be the same. The strategies include choosing a suitable turbulence model, identifying the contaminant modeling method, setting the geometric model, and providing suitable boundary conditions. These strategies should be quantitatively evaluated.

Accurate CFD modelling of airflow cannot be performed without a suitable turbulence model. Liu et al. [21] evaluated several models for predicting airflow in an MD-82 airplane cabin. They found that the large-eddy-simulation model provided the most accurate results, but the computing time was too long. Reynolds-averaged Navier-Stokes (RANS) models were more suitable. Li et al. [12,15] concluded that the Reynolds stress model was not as good as the two-equation RNG k-ε model in predicting the airflow and SF_6 concentration fields in an airplane cabin. Elmaghraby et al. [14] stated that the RNG k-ε model had the lowest errors when simulating the SF_6 concentration inside a three-row cabin mockup of a B767 airplane, compared with the standard k-ε model, the RNG k-ε model, the realizable k-ε model, and the SST k-ω model. However, they only compared the measured and predicted SF_6 concentrations at two points. The above studies were all focused on MV systems. For DV systems, Zhang et al. [26,27] compared the airflow and CO_2 concentration fields predicted by the RNG k-ε model with experimental data. You et al. (2018) [25] predicted the air velocity, air temperature, and contaminant distributions in a Boeing-737 cabin using a hybrid turbulence model. These studies demonstrated that various two-equation RANS models can be used effectively [9]. However, these past studies did not identify the most accurate model.

Lagrangian and Eulerian methods are both popular for modeling particle transportation [9]. The Lagrangian method treats the particles as a discrete phase and calculates the trajectory of each individual particle. A continuous concentration field of particles can be obtained by

tracking a sufficient number of particle trajectories. The Eulerian method treats particles as a continuous phase and solves the corresponding governing transport equations for a scalar. According to previous studies, the two methods provided similar results for particle dispersion, but the computational costs were quite different [28,29]. For a steady state, the calculation time of the Eulerian method was shorter than that of the Lagrangian method because the latter must usually track the trajectories of a large number of particles, generally twice the grid number. Wang et al. (2012) [28] compared the performance of the two methods in a building environment and concluded that the Lagrangian method with the LES and DES models accurately predicted the particle concentration, but the computing cost was very high. The RANS model combined with the Eulerian method was found to provide reasonable and affordable prediction of the particle concentration field at a steady state. However, the particle transmission in airplane cabins has been modeled primarily by the Lagrangian method in previous studies [11,22,23]. The use of the Eulerian method to model particle concentration in airplane cabins still requires a comprehensive evaluation.

Proper simplification of geometry and selection of mesh type and number are important factors in simulation accuracy and computing time. Duan et al. 2015 [19] quantitatively evaluated the accuracy and computing costs for three mesh types and five grid numbers in the simulation of air distribution in an MD-82 first-class cabin. Since the geometry of the first-class cabin was very complex, involving realistic seats, manikins and air diffusers, a hexahedral mesh with a grid number of at least 12 million or a tetrahedral mesh with at least 15 million cells was needed to produce acceptable results. The computing time for each of these simulations would be about 80-90 hours on a computer with 32 cores and a 128 G memory, which is a prohibitively long time for ventilation system analysis. As the geometry of airplane cabins is relatively complex, proper simplification of the geometry is essential for reducing the grid number. Liu et al. 2013 [21] reported that cutting off the aisles at both ends of a first-class cabin could reduce the grid number. The simplification had little influence on the airflow field simulation because there were no heat or momentum sources in the region. However, oversimplification may increase errors in simulations. For example, the seat legs (supporting structure beneath the seats) were commonly simplified during construction of the computational domain of the airplane cabin in previous studies [12-27]. With the DV system, the air is supplied at floor level. The seat legs may be obstacles for the supplied air, reducing the air velocity. The cabin geometry should not be simplified in the same way for different ventilation systems. Unfortunately, no previous studies have quantitatively evaluated the effects of cabin geometry simplification on the accuracy of CFD simulations.

Proper setting of boundary conditions is also essential in CFD modeling [30,31]. For an aircraft cabin, the boundary conditions that most greatly affect the air distribution usually include flow boundary conditions for diffusers, inlet air temperature, and the thermal condition of all surfaces in the cabin. A number of previous CFD simulations in aircraft cabin have set the same inlet flow boundary conditions for all diffusers [13,14,16,23,24,26,27] and the same thermal conditions for the surfaces of all manikins [11,13,14,16,22-24,26,27], while other studies have set the inlet air velocity conditions differently for each diffuser [11,12,15,17,18,22,25]. In some cases, manikins have been divided into head, chest, abdomen, thigh and calf sections, and an average temperature has been used for each section [12,15,17,18,25]. However, the effects of these boundary conditions on the simulation results have not been reported in detail.

Therefore, this study quantitatively evaluated the impact of ventilation system, turbulence model, particle simulation method, geometry simplification, and boundary condition assignment

on airflow and particulate distributions in airliner cabins calculated by CFD. Measurement data [32,33] were used for model validation. The aim of the study was to identify an accurate and affordable method for studying the airflow and particulate contaminant distributions in airliner cabins.

2. Numerical method

2.1. Computational domains

This study constructed a geometric model according to a previously published schematic and field measurement data for a seven-row cabin mockup, as displayed in Fig. 1[32,33]. Fig. 1(a) shows the computational domain with the DV system. There were seven air diffusers on the lower parts of both cabin side walls. Seven exhausts were installed in the middle of the ceiling. Since there was a certain amount of air leakage through the glass door and end door, an air leakage gap with a width of 1 cm was set at the joints according to the contours of these two doors. To connect power cables to the testing instruments in the cabin, a circular opening with a diameter of 10 cm was created in the lower part of the left-hand cabin wall. This opening was also set as an air leak in the geometric model. The air leakage flow rates at the three air leakage positions were determined from the experimental data. For the DV system, the air leakage flow rates were 8%, 2.5% and 2.5% of the total flow rate at the glass door, end door and side wall, respectively. The particle source was located above the head of the manikin in seat B of the fourth row.

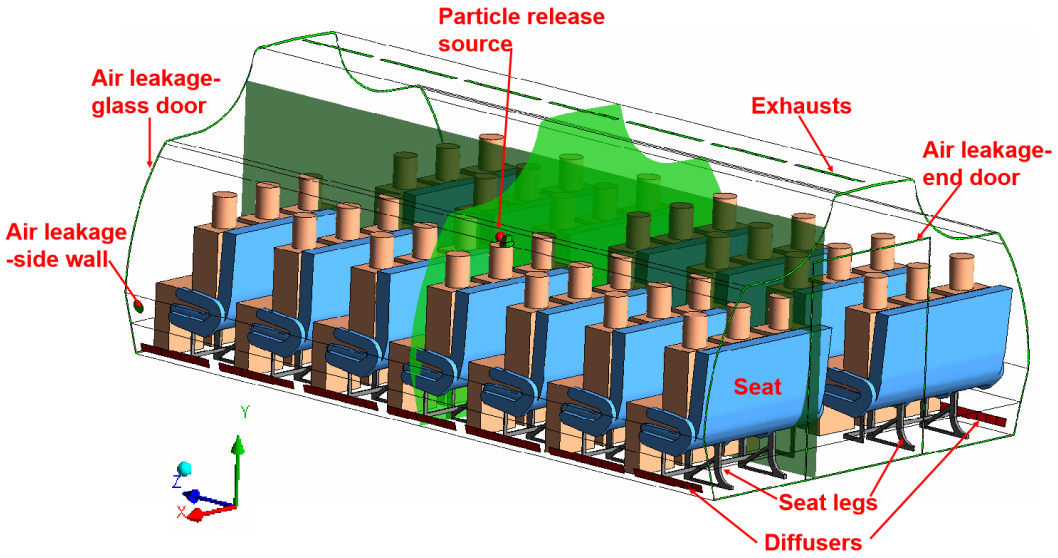

(a)

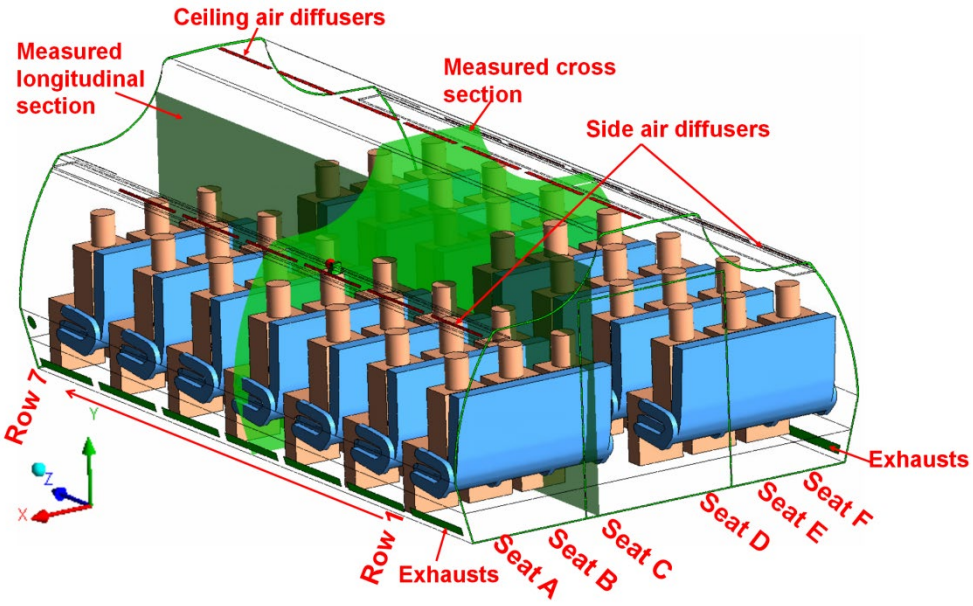

(b)

Fig. 1. Geometric model of the seven-row aircraft cabin: (a) cabin with DV system, and (b) cabin with MV system

Fig. 1(b) shows the computational domain with the MV system. The positions of the particle source, measured sections, and air leakages were the same as with the DV system. The air leakage flow rates were 8%, 4% and 2% at the glass door, end door and side wall, respectively. The locations of the diffusers and exhausts for the DV system were reversed from the locations used for the MV system. In addition, seven diffusers were installed on the shoulders of both side walls. The measurements at the cross section were taken in front of the manikins sitting in the fourth row, and those in the longitudinal section were taken through the middle of the manikins in seat C.

In the experiment, the diffusers in the DV and MV system were simply rectangular openings without any grilles. Aluminum honeycomb cores were installed inside the diffusers to adjust the velocity direction of the supply air. The thickness of the aluminum foil of the honeycomb was as thin as 0.04 mm, and the effective area coefficient of the air supply opening was 98%. Therefore, this study used rectangular openings to represent the diffusers and scaled down all openings to keep the same effective area as the experimental mockup. The method ensures that the inlet velocity, mass flow rate and momentum flux are the same as the experimental data.

Since the air diffusers were located in the lower part of the cabin with the DV system, the geometric obstacles under the seats may have affected the air distribution inside the cabin. Therefore, this study evaluated the effect of the seat legs on the airflow.

2.2. Boundary conditions

This study set the velocity inlet and air temperature for the diffusers and the outflow for the exhausts and air leakages. For the surface temperatures, measured data was used. The modeled particles had a diameter of 1 μm, and a density of about 915 kg/m^3. The mass flow rate of the particle source was 0.00462 kg/s. The particle deposition rate of particles with a diameter of 1.0 μm in the fully occupied aircraft cabin was about 0.0000515 s^{-1} estimated by the empirical deposition equations proposed by You and Zhao [34]. However, the air change rate in the aircraft cabin was about 0.013 s^{-1}, which was three orders of magnitude higher than the particle

deposition rate. Therefore, particle deposition has little effect on the particle distribution in the aircraft cabin, which can be neglected [20].

2.3. Turbulence models

This investigation used the standard k-ε model, the RNG k-ε model, the realizable k-ε model, and the SST k-ω model to study the airflow and particle dispersion in the seven-row aircraft cabin. The governing equations for all four turbulence models can be written in a general form:

$$\rho \frac{\partial \bar{\Phi}}{\partial t} + \rho \bar{u}_i \frac{\partial \bar{\Phi}}{\partial x_i} - \frac{\partial}{\partial x_i}\left[\Gamma_{\phi,eff} \frac{\partial \bar{\Phi}}{\partial x_i}\right] = S_\phi \quad (1)$$

where ϕ represents the flow variables, $\Gamma_{\phi,\text{eff}}$ the effective diffusion coefficient, and S_ϕ the source term. Table A1 presents key information for the four turbulence models. A more detailed description of these turbulence models can be found in the user manual of the ANSYS Fluent Version 19.0 software program [35].

2.4. Eulerian method

This study used the Eulerian method to calculate the particle concentration in the cabin. The concentration was calculated by the following transport equation [36]:

$$\nabla \cdot \left(\rho\left(\vec{u} + \overrightarrow{V_S}\right)C\right) = \nabla \cdot (\Gamma \nabla C) + S_C$$

where $\overrightarrow{V_S}$ is the settling velocity of particles, ρ the density of air, C the concentration of particles, Sc the generation rate of the particle source, and Γ the effective particle diffusivity:

$$\Gamma = \rho\left(D + v_p\right)$$

Here D is the Brownian diffusivity of particles and ν_p the particle turbulent diffusion coefficient. The D is negligible compared with ν_p in a turbulent flow when the particle size is larger than 0.01 μm. The ν_p is equal to the gas diffusion coefficient ν_t when the Stokes number of a particle approaches zero in a homogeneous turbulent flow [37,38]. As long as the particle Stokes number is low, this relation holds, although real airflows may not satisfy the assumption of homogeneity [39].

The settling velocity of a particle, derived by equating the fluid drag force on the particle with the gravitational force, can be expressed as:

$$V_s = \frac{\rho_p d_p^2 g C_c}{18\mu_a} \quad (4)$$

where ρ_p is the particle density, d_p the particle diameter, μ_α the air viscosity, g the gravitational acceleration, and C_c the Cunningham correction factor. This factor can be expressed as:

$$C_c = 1 + \frac{2\lambda}{d_p}(1.257 + 0.4\exp(-1.1 d_p/2\lambda)) \quad (5)$$

where λ is the mean free path of air molecules, which is 0.066 μm when the air temperature is 20 ℃ and the pressure is 0.1 MPa.

2.5. Numerical schemes

This study used the commercial CFD software ANSYS FLUENT 19.0 to perform all the numerical calculations. The Eulerian model was realized by implementing a user-defined function in ANSYS Fluent. This study employed the Boussinesq assumption to account for the buoyancy effect. For the k-ε models, it was necessary to use the wall function to solve the fluid velocity in the viscous sublayer near the wall. Since the surface-averaged y+ was less than 10 in this study, the enhanced wall function was used [13,19,21]. This investigation used the finite volume method to discretize the governing equations and the SIMPLE algorithm to couple the pressure and velocity. The PRESTO! scheme was adopted for pressure discretization, and

second-order upwind was used for iterations for all variables except pressure, in order to achieve higher accuracy. Convergence was reached when the sum of the normalized residuals for all the cells became less than 10^{-6} for energy and 10^{-3} for all the other variables. Since the particle concentration was a scalar equation computed from the convergent flow field, the required computing time was short.

2.6. Grid independence tests

This study performed a grid-independence test for grid numbers of 2.87 million, 5.77 million, and 11.72 million. Fig. 2 compares the air velocity profiles with the DV system at two horizontal lines and two vertical lines on the cross section. The results with 5.77 million cells were nearly the same as those with 11.72 million cells, and were close to the experimental data. Therefore, this study selected the 5.77-million-cell mesh for further investigation with the DV system, as shown in Fig. 3(a). The cell size for the diffusers was about 10 mm, for the dummies and seats about 25 mm, and for the rest of the space about 50 mm. The size change was controlled to be less than 20% to reduce numerical diffusion. The same cell size as the DV system was used to generate the mesh for the MV system, as shown in Fig. 3 (b).

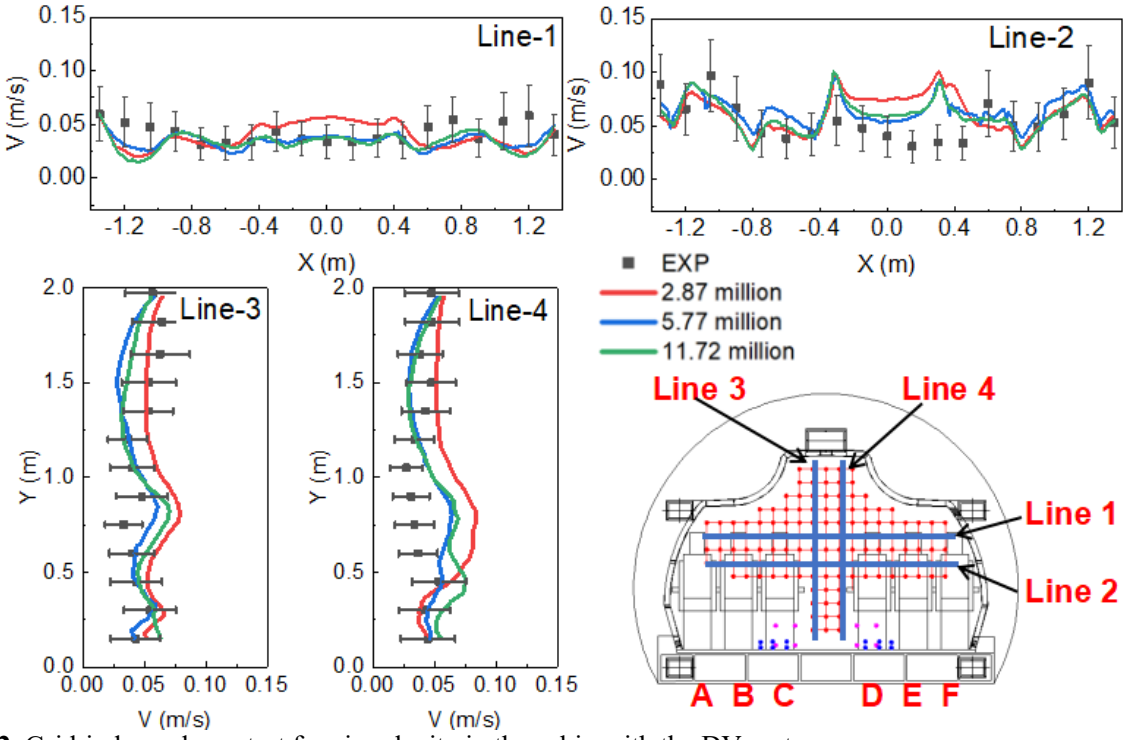

Fig. 2. Grid-independence test for air velocity in the cabin with the DV system.

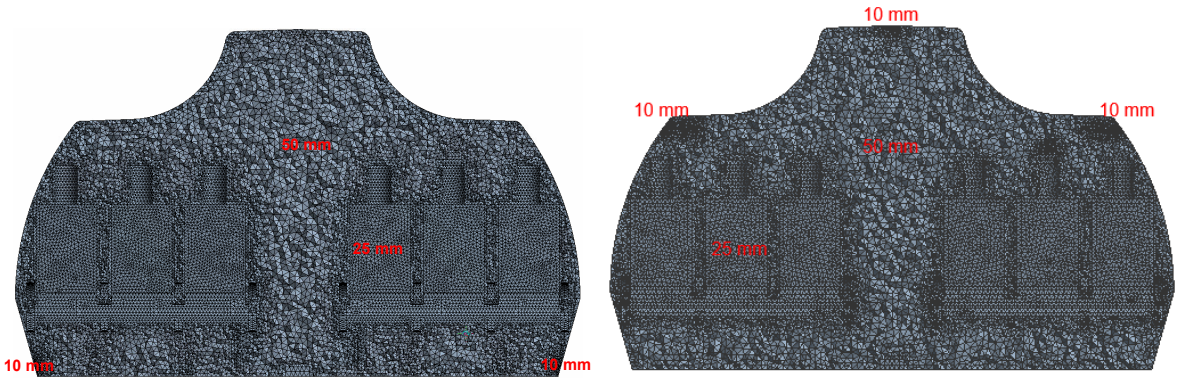

(a) (b)

Fig. 3. Mesh distribution selected for the cabin with (a) the DV system (5.77 million cells) and (b) the MV system (5.97 million cells)

2.7. Criteria for validating the CFD results

This study qualitatively and quantitatively compared our CFD results with the experimental data to evaluate the CFD performance. The quantitative comparisons used the normalized root-mean-square error (RMSE) [12] to describe the discrepancies with the data:

$$RMSE(C_{pi}, C_{mi}) = \sqrt{\frac{\sum_{i=1}^{n}\left(C_{pi} - C_{mi}\right)^2}{\sum_{i=1}^{n} C_{mi}^{\ 2}}} \tag{6}$$

where C_{pi} and C_{mi}, respectively, represent the predicted results and measured data, such as air velocity, air temperature, and particle concentration at certain locations. This study used dimensionless variables that were defined as:

$$V^* = \frac{V_{local}}{\overline{V}} \quad T^* = \frac{T_{local} - T_{in}}{T_{out} - T_{in}} \quad C^* = \frac{C_{local} - C_{in}}{C_{out} - C_{in}},\ C_{in} = 0 \tag{7}$$

where $\overline{V}$ is the average velocity at all the measured locations, and V_{local} ,T_{local} and C_{local} are the air velocity, air temperature and particle concentration, respectively, at a given location. Meanwhile, T_{in} and C_{in} are the air temperature and particle concentration, respectively, from the diffusers, and T_{out} and C_{out} are the air temperature and particle concentration, respectively, at the exhausts.

3. Results

3.1. Comparison of turbulence models

In order to select a suitable turbulence model, this study took the DV system as an example and compared the results predicted by different turbulence models with the measured data. As shown in Fig. 4, all four turbulence models predicted an airflow distribution consistent with the experimental data, generally in the form of bottom-up flow. Nevertheless, there were some differences between the results of the different models at some measuring points. In particular, the velocity magnitude and direction predicted by the SST k-ω model deviated more from the experimental data than did those predicted by the other three k-ε models at most of the measuring points in the cross section. Among the three k-ε models, the results of the standard k-ε

model and realizable k-ε model were similar, while the results of the RNG k-ε model were somewhat different.

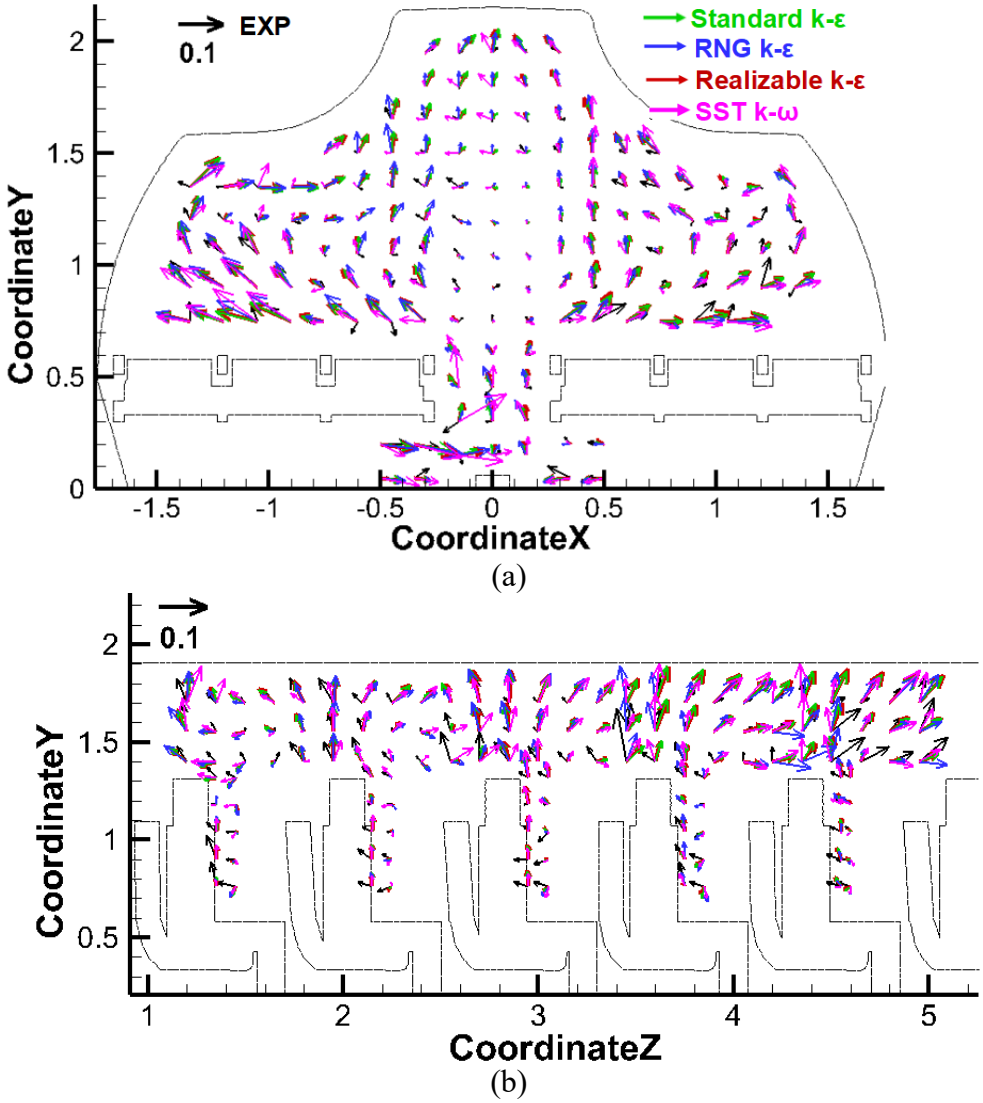

Fig. 4. Qualitative comparison of velocity field with DV system predicted by different turbulence models in (a) the cross section and (b) the longitudinal section.

Fig. 5 compares the predicted and measured temperature profiles on 8 lines of the cross and longitudinal sections. The temperature field predictions by the three k-ε models were similar and agreed well with the experimental data. The temperatures predicted by the SST k-ω model were 0.5 ℃ lower than the experimental data and the results of the three k-ε models.

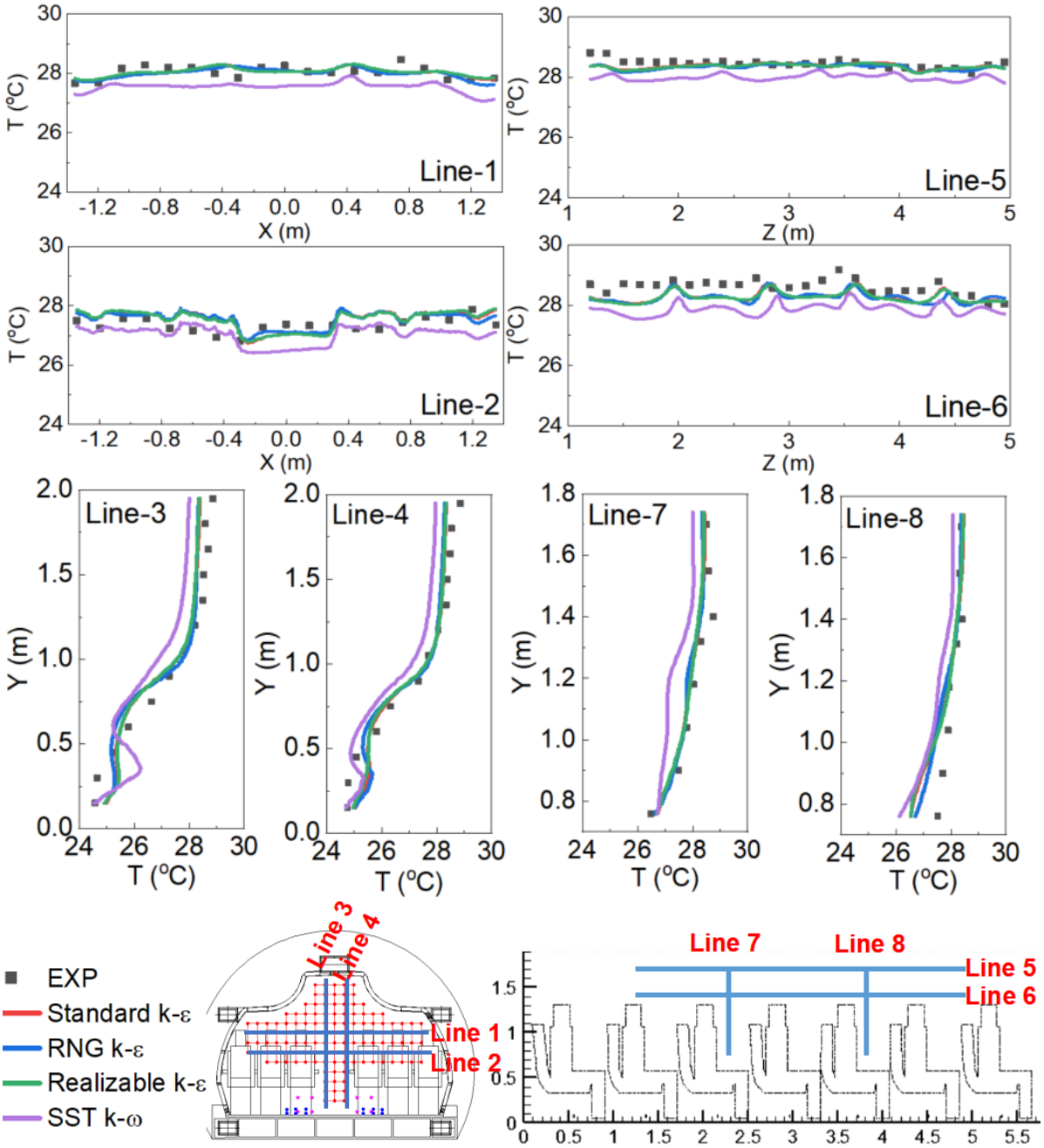

Fig. 5. Comparison of the predicted and measured temperature profiles under the DV system.

To provide a quantitative evaluation of the four turbulence models, Table 1 summarizes the calculated RMSE values using the velocity, temperature and particle concentration predicted by the four different two-equation turbulence models. For the velocity and temperature fields, the three k-ε models provided similar RMSE values. For the particle concentration, the RMSE of the realizable k-ε model was similar to the best data predicted by SST k-ω model, which was 2.6% better than the standard k-ε model and 7.2% better than the RNG k-ε model. The velocity and temperature fields predicted by SST k-ω model deviated the most from the experimental data. Overall, among the four turbulence models, the realizable k-ε model agreed the most closely with the measurement data.

Table 1
Index RMSE values for evaluating the velocity, temperature and particle concentration predicted by the four two-equation turbulence models.

DV system	Velocity	Temperature	Concentration
Standard k-ε	0.426	0.078	0.941
RNG k-ε	0.425	0.082	0.987
Realizable k-ε	0.426	0.079	0.915
SST k-ω	0.492	0.091	0.908

3.2. Comparison of geometry simplification

This study evaluated the effect of seat-leg removal on the accuracy of airflow field prediction for both the MV and DV systems. As shown in Fig. 6(a), the simulated air velocity under the seat in the DV system without the seat legs was much higher than the measured velocity, which also increased the simulated velocity throughout the whole section. Since the diffusers in the DV system were installed in the lower part of the cabin, the seat legs were important. However, Fig. 6(b) depicts a smaller improvement with the seat legs for the MV system because the seat legs were in the recirculation zone. Table 2 lists the calculated RMSE values with and without seat legs. With the seat legs, the simulation accuracy was moderately higher. The results again demonstrated a more significant improvement with seat legs for the DV system than for the MV system. The modest improvement came at a price. The simulations with the seat legs used about one million cells more than the case without seat legs, and the computing time was 20% longer.

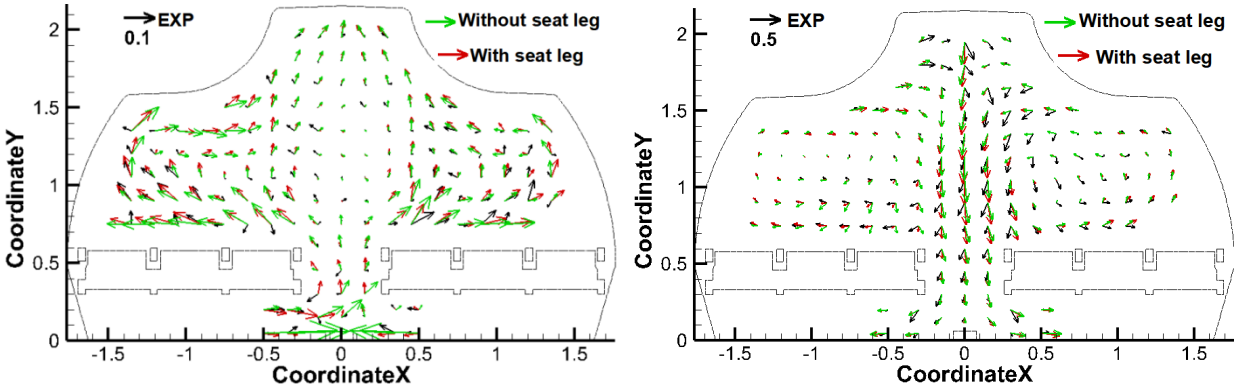

Fig. 6. Comparison of simulated and measured airflow distribution with and without seat legs in a cross section of the cabin: (a) for the DV system and (b) for the MV system.

Table 2
RMSE values for evaluating air velocity, air temperature and particle concentration with and without the consideration of seat legs for the DV and MV systems

		Air velocity	Air temperature	Particle concentration
DV	With seat legs	0.426	0.079	0.915
	Without seat legs	0.518	0.119	0.931
MV	With seat legs	0.455	0.202	0.551
	Without seat legs	0.473	0.223	0.579

3.3. Comparison of different assignment methods of boundary conditions

3.3.1 Inlet boundary condition

Previous comparisons between the numerical and experimental data of the airflow and contaminant distribution in airplane cabin were unsatisfactory. Proper setting of boundary conditions helps improving the accuracy of CFD simulations. The previous experimental study [32,33] provided measurement data for velocity magnitude, velocity direction and turbulence intensity at seven measuring points for each diffuser in the DV system and the MV system. Since the uniformity of velocity among diffusers was similar in the two ventilation systems, this study took the DV system as an example and designed three cases to evaluate the effect of different assigned velocity boundary conditions on simulation accuracy. In case DV1, the velocity magnitude, velocity direction and turbulence intensity at each diffuser were the average values for the seven diffusers on the same side. In case DV2, the velocity boundary conditions for each diffuser, were the average data for the seven measuring points on that diffuser. In case DV3, each diffuser was divided into seven parts, and the velocity boundary was specified as the experimental data at its seven measuring points.

Table 3 lists the RMSE values for evaluating velocity, temperature and particle concentration in cases DV1, DV2 and DV3. The boundary conditions assigned to case DV3 was the most detailed and to case DV1 the simplest. The results show that more detailed assignment of velocity boundary conditions leads to more accurate modeling of velocity, temperature and particle concentration. The influence was most obvious in the prediction of the velocity field, and least obvious for temperature. Assigning the velocity at seven points for each diffuser could reduce the RMSE by 8.9% for velocity, 4.6% for particle concentration and 0.4% for temperature, compared to using the average velocity boundary conditions for the seven diffusers. In addition, the difference between cases DV3 and DV2 was greater than that between cases DV2 and DV1. The reason was that the standard deviation of the average velocity for the seven diffusers on the same side was less than that of the velocity for the seven measuring points on each diffuser. Therefore, it is recommended that the uniformity of the velocity distribution on the diffusers be taken into account when the inlet velocity boundary conditions are specified in the simulation. The quantitative comparison in this study shows the effect of different assignments of boundary condition on the simulation accuracy, which helps CFD engineers to make a balance between more simple boundary and higher simulation accuracy.

Table 3
RMSE values for evaluating velocity, temperature and particle concentration in cases with three different assignments of velocity boundary conditions in the DV system

	Velocity	Temperature	Concentration
Case DV1	0.515	0.083	0.961
Case DV2	0.486	0.082	0.958
Case DV3	0.426	0.079	0.915

3.3.2 Wall temperature boundary condition

Since the heated manikins were the major sources of heat in the aircraft cabin, the surface temperatures of the manikins may have affected the temperature and airflow fields. The average temperatures of all the manikins were 30.01 ℃ in the DV system and 30.12 ℃ in the MV system. The temperatures of the 42 manikins were more uniform in the DV system than in the MV

system. The difference between the maximum and minimum values was 0.14 ℃ in the DV system and 1.29 ℃ in the MV system. Since the temperatures of the 42 manikins were nearly the same in the DV system, the average temperature of 30.01 ℃ was set as the temperature boundary for all the manikins. For the MV system, this study compared two cases with different assignments of manikin temperatures. Case MV1 adopted the average temperature of 30.12 ℃, and case MV2 specified the temperature boundary for each manikin according to the measured data.

To evaluate the effect of the manikins' temperature boundary on the predicted airflow, temperature and particle concentration fields, Table 4 compares the RMSE values calculated for cases MV1 and MV2. Among the 42 manikins, the standard deviation of surface temperature was 0.4 ℃, and the difference between the maximum and minimum value was 1.3 ℃. As shown in Table 4, the RMSE values for case MV2 were 5.1%, 2.5% and 9.8% better than those for case MV1 for the velocity field, temperature field and particle concentration field, respectively. For more accurate simulation results, it would be better to assign the surface temperature separately for each manikin according to the measured data when the surface temperature deviation among manikins is greater than 1 ℃.

Table 4
RMSE values for evaluating velocity, temperature and particle concentration in the two cases with different assignments of manikin surface temperature in the MV system

	Velocity	Temperature	Concentration
Case MV1	0.506	0.227	0.649
Case MV2	0.455	0.202	0.551

3.3.3. Outlet boundary condition

In the past, it was usually considered that the distribution of return air flow rate at the exhausts had little influence on the flow field in an airplane cabin. Few experimental studies reported the velocity distribution at the exhausts, and current numerical investigations typically set a uniform outflow in the modeling process. However, in the validation experiments for the DV system in the present study, the resistance at the seven exhausts varied greatly because filters with different thicknesses were used to balance the supply air flowrate under the MV system. In the DV system, 8%, 2.5% and 2.5% of the total supply air exited through air leakage at the glass door, the end door and the side wall, respectively. Table 5 shows the distribution of the remaining 87% of the airflow through the seven exhausts at different positions. Along the positive direction of the Z axis, each exhaust was divided into five equal parts that were labeled from No. 1 to No. 5. The data indicate that the outflow rates at the exhausts near the cabin doors were larger than at the exhausts in the middle of the cabin. The outflow rate at Exhaust_7 was the highest. This study compared two cases, with uniform and non-uniform outflow boundary conditions, to demonstrate the effect of outflow on the airflow distribution inside the aircraft cabin. The outflow rates at the exhausts were set in accordance with the measured data shown in Table 5 for the non-uniform case. For the uniform case, 87% of the airflow was uniformly distributed across the exhausts. The predicted results show that the RMSE values for the non-uniform case were 3.6% and 4.4% better than those for the uniform case for the velocity and particle concentration fields, respectively. The airflow field in the upper region of the cabin (above 1.3 m) was affected by the different outlet boundary conditions. The uniform case over-predicted the airflow rates through the exhausts in the middle of the cabin, leading to over-prediction of the air velocity near

the exhausts. For more accurate simulation results, it is recommended that the airflow rates at the exhausts and the air leakage be verified.

Table 5
Distribution of airflow through different exhausts under the DV system

Exhaust in DV system	No. 1	No. 2	No. 3	No. 4	No. 5
Exhaust_1	2.95%	2.84%	2.79%	2.49%	2.18%
Exhaust_2	1.60%	1.53%	1.53%	1.23%	0.97%
Exhaust_3	0.85%	0.89%	0.95%	0.89%	0.83%
Exhaust_4	0.86%	0.88%	0.90%	0.90%	0.95%
Exhaust_5	2.08%	1.72%	1.58%	1.37%	1.05%
Exhaust_6	1.46%	1.37%	1.29%	2.73%	3.13%
Exhaust_7	7.08%	7.81%	8.43%	8.43%	8.47%

4. Discussion

This section qualitatively compares the predicted and measured data for the DV and MV systems. Fig. 7(a) and (b) present the measured and simulated airflow patterns in the DV system and the MV system, respectively. The air velocity in the cabin under the DV system was quite low overall, and was generally below 0.1 m/s. Under the MV system, the airflow velocity varied greatly from one position to another, reaching 0.5 m/s in some locations. Forced convection was dominant in the MV system, while natural convection was dominant in the DV system. Because the overall velocity was relatively low, larger instrumental error during the measurement was unavoidable and led to some deviations between the measured and predicted results. The simulation of velocity direction was more accurate for the MV system than for the DV system. In general, the predicted airflow features were similar to the measured results for both ventilation systems. Under the DV system, the supply air from the diffusers on both sides of the cabin met in the aisle and then rose upward, driven by thermal buoyancy. The general airflow direction was upward, and no significant vortices were formed under the DV system. Under the MV system, the supply air from the right side, left side and ceiling collided in the upper region of the aisle and then flowed downward to the floor, forming two large vortices on the two sides of the cabin. In the aisle of the cabin, the measured downward airflow turned slightly to the left and gradually decreased, while the predicted airflow direction was essentially straight down to the floor. In addition, the simulated attenuation of the velocity magnitude was not as obvious as in the measured data. During the measurements, the height of the diffusers may have differed between the left and right sides, leading to a left-right skewing of the airflow field in the experiment. However, it would be difficult to establish the deviation in geometric position in complete accordance with the actual situation in the simulation. Therefore, there was a certain deviation between the predicted and measured airflow field.

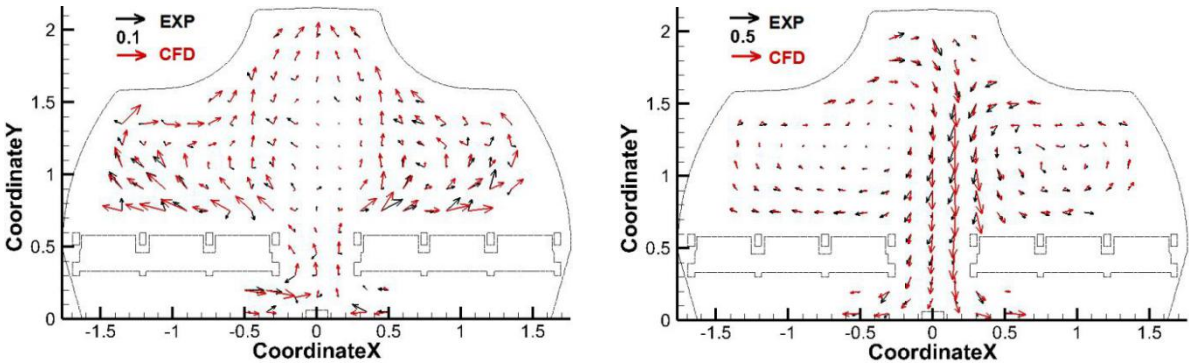

Fig. 7. Qualitative comparison of velocity field between experimental and simulation results under (a) the DV system and (b) the MV system

Fig. 8 compares the measured and predicted temperature field under the DV and MV systems. Temperature stratification and symmetry can be observed under the DV system. Because there was no collision of strong airflow in the area above the seats in the DV system, the airflow field and temperature field were relatively stable. In the MV system, two large eddies on the left and right sides mixed the airflow and produced a uniform temperature field around the passengers. The low temperature in the aisle was due to the lower-temperature jet flow from the diffusers on the ceiling. Because the two vortices constantly collided with and pressed against each other, the airflow field in the mixed ventilation mode was relatively unstable and asymmetric. The measured low-temperature jet flow skewed to the right side, while the predicted jet skewed to the left side, leading to a higher predicted temperature in the vortex on the right side. However, the overall predicted temperature field agreed well with the experimental results, especially under the DV system.

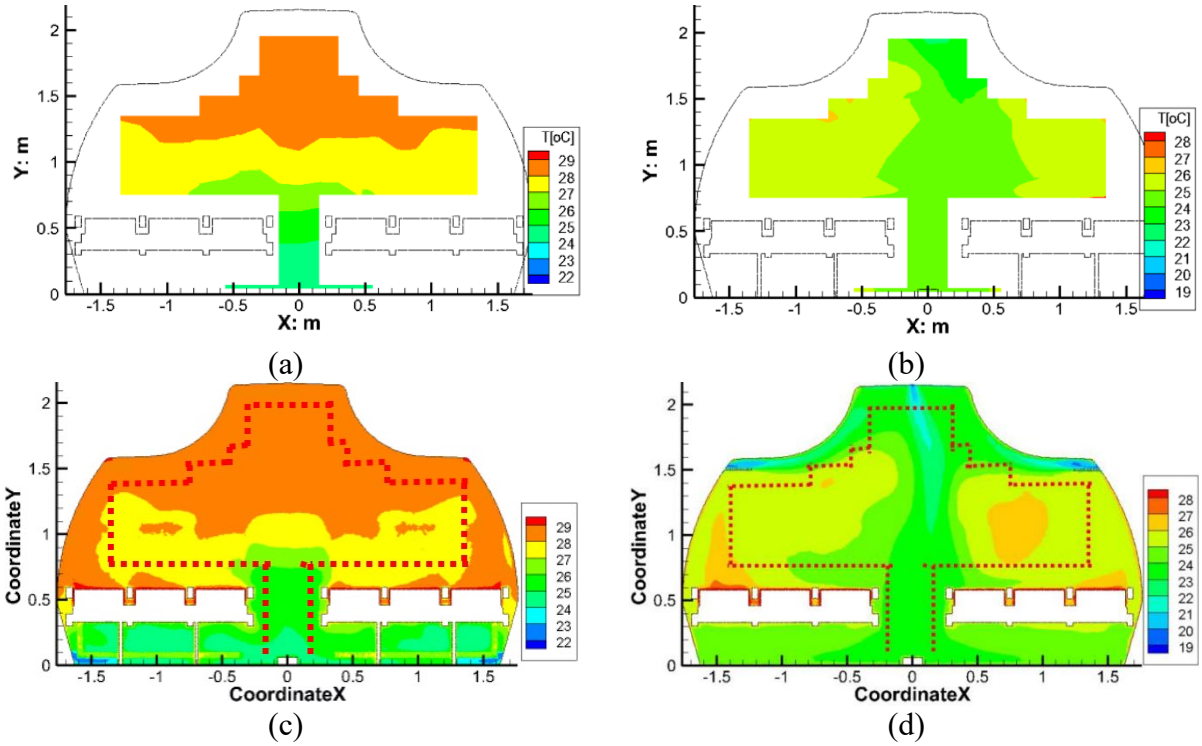

Fig. 8. Qualitative comparison of temperature field between experimental and simulation results: (a) measured data for DV system, (b) measured data for MV system, (c) predicted data for DV system, and (d) predicted data for MV system

Fig. 9 compares the predicted and measured concentration field for particles with diameter of 1 μm under the DV and MV systems. Since the air was flowing from the lower region to the upper region of the cabin under the DV system, the particles were moving directly with the airflow from the source to the exhausts. There was little spreading of particles to the breathing zones of other passengers. The DV system exhibited excellent performance in minimizing the cross-transmission of airborne particles. Under the MV system, the particles were released from the source, moved upward with the supply air, merged with the supply air from the ceiling, and were then carried into the large vortex on the right. The measured aisle airflow skewed to the left and brought some particles to the left. The particle diffusion range under the MV system was larger than under the DV system. The predicted diffusion range for the particles was slightly smaller than the measured results. The airflow was unsteady during the experiments, and the fluctuation of the air flow augmented the particle diffusion. The movement of the 3D robot and the measuring instruments could have created certain disturbances in the flow field during the experiment and thus further diffusion of the particles. In this study, the simulation of particles was based on the predicted steady-state flow field, leading to insufficient prediction of the diffusion effect to some extent, especially under the DV system with low air velocity.

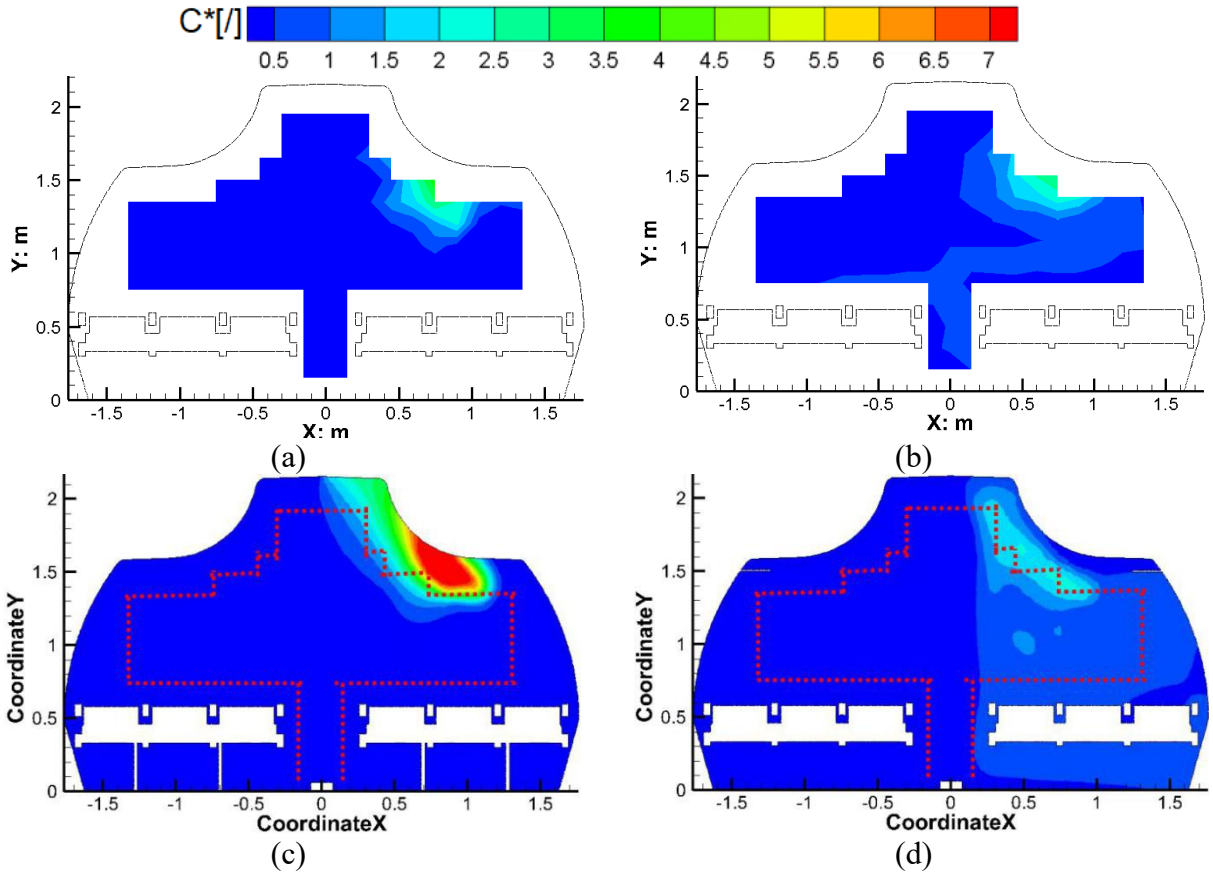

Fig. 9. Qualitative comparison of the concentration field for 1 μm particles between experimental and simulation results: (a) measured data for DV system, (b) measured data for MV system, (c) predicted data for DV system, and (d) predicted data for MV system

5. Conclusions

The complex geometry and airflow characteristics in airplane cabins pose a challenge to accurate numerical CFD validation. This study quantitatively evaluated the impact of ventilation system, turbulence model, particle simulation method, geometry simplification, and boundary condition assignment on the CFD simulation of airflow and particulate contaminant fields in airliner cabins under mixing ventilation and displacement ventilation systems. This investigation led to the following basic conclusions and findings:

Among four turbulence models, the standard k-ε, RNG k-ε, realizable k-ε and SST k-ω, the results predicted by the realizable k-ε model agreed most closely with the experimental data. The steady Eulerian method provided a reasonable prediction of the particle concentration field with low computing cost.

Adding the seat legs to the geometric model could obviously improve the simulation accuracy for the DV system, while it was not recommended for the MV system because of the high increase of computing cost and little improvement of accuracy.

To improve the simulation accuracy, it is recommended to assign more detailed boundary, such as inlet velocity, surface temperature of manikins.

The simulation of velocity direction was more accurate under the MV system, and insufficient prediction of the diffusion effect under the DV system was more obvious. Under the DV system, there was noticeable temperature stratification; the temperature field was more stable and the simulation results for temperature were more accurate.

References

[1] C. A. Mboreha, C. S. Abdallah, G. Kumar, Risk and prevention of COVID-19 in a commercial aircraft cabin: An overview, Int. J Appl Technol. 5(3) (2020) 661-670.

[2] Q. Chen, Can we migrate COVID-19 spreading risk? Front. Environ. Sci. Eng. 15(3) (2021) 35.

[3] J. Fišer, M. Jícha, Impact of air distribution system on quality of ventilation in small aircraft cabin, Build Environ. 69 (2013) 171-182.

[4] J. Maier, C. Marggraf-Micheel, T. Dehne, J. Bosbach, Thermal comfort of different displacement ventilation systems in an aircraft passenger cabin, Build Environ. 111 (2017) 256-264.

[5] F. Juli, Z. Qiongyao, A review about thermal comfort in aircraft, J Therm Sci. 28(02), (2018) 13-27.

[6] R. You, Chao-Hsin Lin, D. Wei, Q. Chen, Evaluating the commercial airliner cabin environment with different air distribution systems, Indoor Air 29 (2019) 840-853.

[7] Y. Zhang, J. Liu, J. Pei, J. Li, C. Wang, Performance evaluation of different air distribution systems in an aircraft cabin mockup, Aero. Technol. 70 (2017) 359-366.

[8] A. M. Farag, E. E. Khalil, Numerical analysis and optimization of different ventilation systems for commercial aircraft cabins, IEEE (2015) 1-12.

[9] H. A. Elmaghraby, Y. W. Chiang, A. A. Aliabadi, Ventilation strategies and air quality management in passenger aircraft cabins: A review of experimental approaches and numerical simulations, Sci. Technol. Built Environ. (2017) 1-16.

[10] H. Chen, X. Zhou, Z. Feng, S. J. Cao, Application of polyhedral meshing strategy in indoor environment simulation: Model accuracy and computing time, Indoor Built Environ. 0 (2021) 1-13.

[11] Z. Zhang, X. Chen, S. Mazumdar, T. Zhang, Q. Chen, Experimental and numerical investigation of airflow and contaminant transport in an airliner cabin mockup. Build. Environ. 44(1) (2009) 85-94.

[12] M. Li, Y. Yan, B. Zhao, J. Tu, J. Liu, F. Li, C. Wang, Assessment of turbulence models and air supply opening models for CFD modelling of airflow and gaseous contaminant distributions in aircraft cabins, Indoor Built Environ. 27(5) (2018) 606-621.

[13] Y. Zhao, Z. Liu, X. Li, M. Zhao, Y. Liu, A modified turbulence model for simulating airflow aircraft cabin

environment with mixed convection, Build. Simul. 13 (2020) 665-675.
[14] H. A. Elmaghraby, Y. W. Chiang, A. A. Aliabadi, Are aircraft acceleration-induced body forces effective on contaminant dispersion in passenger aircraft cabins? Sci. Technol. Built Environ. 25(7) (2019) 858-872.
[15] F. Li, J. Liu, J. Ren, X. Cao, Predicting contaminant dispersion using modified turbulent Schmidt numbers from different vortex structures, Build. Environ. 130 (2018b) 120-127.
[16] Y. Yan, X. Li, Y. Shang, J. Tu, Evaluation of airborne disease infection risks in an airliner cabin using the Lagrangian-based Wells-Riley approach, Build. Environ. 121 (2017) 79-92.
[17] F. Li, J. Liu, J. Ren, X. Cao, Y. Zhu, Numerical investigation of airborne contaminant transport under different vortex structures in the aircraft cabin, Int. J. Heat Mass Tran. 96, (2016) 287-295.
[18] M. Li, B. Zhao, J.Tu, Y. Yan, Study on the carbon dioxide lockup phenomenon in aircraft cabin by computational fluid dynamics, Building Simul. 8 (2015) 431-441.
[19] R. Duan, W. Liu, L. Xu, Y. Huang, X. Shen, C. H. Lin, J. Liu, Q. Chen, Mesh type and number for the CFD simulations of air distribution in an aircraft cabin, Numer. Heat Tr. B Fund. 67(6) (2015) 489-506.
[20] C. Chen, W. Liu, F. Li, C. H. Lin, J. Liu, J. Pei, Q. Chen, A hybrid model for investigating transient particle transport in enclosed environments, Build. Environ. 62 (2013) 45-54.
[21] W. Liu, J. Wen, C. H. Lin, J. Liu, Z. Long, Q. Chen, Evaluation of various categories of turbulence models for predicting air distribution in an airliner cabin, Build. Environ. 65 (2013) 118-131.
[22] M.Wang, C. H. Lin, Q. Chen, Determination of particle deposition in enclosed spaces by Detached Eddy Simulation with the Lagrangian method, Atmos. Environ. 45(30) (2011) 5376-5384.
[23] M. P. Wan, G. N. Sze To, C. Y. H. Chao, L. Fang, A. Melikov, Modeling the fate of expiratory aerosols and the associated infection risk in an aircraft cabin environment, Aero. Sci. Technol. 43(4) (2009) 322-343.
[24] W. Yan, Y. Zhang, Y. Sun, D. Li, Experimental and CFD study of unsteady airborne pollutant transport within an aircraft cabin mock-up, Build. Environ. 44(1) (2009) 34-43.
[25] R. You, Y. Zhang, X. Zhao, C. H. Lin, D. Wei, J. Liu, Q. Chen, An innovative personalized displacement ventilation system for airliner cabins, Build. Environ. 137 (2018) 41-50.
[26] T. Zhang, P. Li, Y. Zhao, S. Wang, Various air distribution modes on commercial airplanes—Part 2: Computational fluid dynamics modeling and validation, HVAC&R Res. 19(5) (2013) 457-470.
[27] T. Zhang, P. Li, S. Wang, A personal air distribution system with air terminals embedded in chair armrests on commercial airplanes, Build. Environ. 47 (2012) 89-99.
[28] M. Wang, C. H. Lin, and Q. Chen, Advanced turbulence models for predicting particle transport in enclosed environments, Build. Environ. 47 (2012) 40-49.
[29] Z. Zhang, Q. Chen, Comparison of the Eulerian and Lagrangian methods for predicting particle transport in enclosed spaces, Atmos. Environ. 41 (2007) 5236-5248.
[30] J. Srebric, V. Vukovic, G. He, X. Yang, CFD boundary conditions for contaminant dispersion, heat transfer and airflow simulations around human occupants in indoor environments, Build. Environ. 43(3) (2008) 294-303.
[31] Q. Chen, J. Srebric, A procedure for verification, validation, and reporting of indoor environment CFD analyses, HVAC&R Res. 8(2) (2002) 201-216.
[32] M. Liu, D. Chang, J. Liu, S. Ji, C. H. Lin, D. Wei, Z. Long, T. Zhang, X. Shen, Q. Cao, X. Li, X. Zeng, H. Li, Experimental investigation of air distribution in an airliner cabin mockup with displacement ventilation, Build. Environ. 191 (2021) 107577.
[33] X. Li, T. Zhang, M. Fan, M. Liu, D. Chang, D. Wei, C. H. Lin, S. Ji, J. Liu, X. Shen, Z. Long, Experimental evaluation of particle exposure at different seats in a single-aisle aircraft cabin, Build. Environ. (2021) 108049.
[34] R. You, B. Zhao, A simplified method for assessing particle deposition rate in aircraft cabins, Atmos. Environ. 67 (2013) 80-84.
[35] ANSYS, ANSYS Fluent 19.0 Documentation, ANSYS, Inc., Lebanon, NH, (2010).
[36] C. Chen, W. Liu, C.H. Lin, Q. Chen, Comparing the Markov chain model with the Eulerian and Lagrangian models for indoor transient particle transport simulation, Aero. Sci. Technol. 49 (2015) 857-871.
[37] J.O. Hinze, Turbulence, 2nd Edition, pp. 1975, 460-471, New York: McGraw-Hill.

[38] C.M. Tchen, Mean value and correlation problems connected with the motion of small particles suspended in a turbulent fluid, Ph. D. thesis, Delft. (1947).
[39] A.C.K. Lai, W.W. Nazaroff, Modeling indoor particle deposition from turbulent flow onto smooth surfaces, J Aero. Sci. 31(4) (2000) 463-476.

Appendix.

Table A1 Coefficients and source terms for the governing equations

		ϕ	$\Gamma_{\phi,eff}$	S_ϕ	Constants
Reynolds -averaged variables	Continuity	1	0		
	Momentum	u_j	$\mu+\mu_t$	$-\frac{\partial p}{\partial x_i}+\frac{\partial}{\partial x_j}\left[(\mu+\mu_t)\frac{\partial u_j}{\partial x_i}\right]$	
	Temperature	T	$\frac{\mu}{Pr}+\frac{\mu_t}{\sigma_T}$	S_T	
Standard k-ε		k	$\mu+\frac{\mu_t}{\sigma_k}$	$G_k+G_b-\rho\varepsilon$	$\mu_t=\rho C_\mu\frac{k^2}{\varepsilon}$, $G_K=\mu_t S^2$,$S=\sqrt{2S_{ij}S_{ij}}$, $\sigma_\varepsilon=1.3$,$C_\mu=0.09$, $G_b=\beta g_i\frac{\partial\mu_t}{\partial\sigma_{T,t}}\frac{\partial\bar{T}}{\partial x_i}$, $C_{1,\varepsilon}=1.44$, $C_{2,\varepsilon}=1.92$, $\sigma_k=1.0$,
		ε	$\mu+\frac{\mu_t}{\sigma_\varepsilon}$	$C_{1\varepsilon}G_k\frac{\varepsilon}{k}-C_{2\varepsilon}\rho\frac{\varepsilon^2}{k}$	
RNG k-ε		k	$\mu+\frac{\mu_t}{\sigma_k}$	$G_k+G_b-\rho\varepsilon$	$\mu_t=\rho C_\mu\frac{k^2}{\varepsilon}$,$G_K=\mu_t S^2$, $S=\sqrt{2S_{ij}S_{ij}}$ $G_b=\beta g_i\frac{\partial\mu_t}{\partial\sigma_{T,t}}\frac{\partial\bar{T}}{\partial x_i}$, $R_\varepsilon=\frac{C_\mu\rho\eta^3(1-\eta/\eta_0)}{1+\beta\eta^3}\frac{\varepsilon^2}{k}$,$\eta\equiv Sk/\varepsilon$, $\eta_0=4.38$,$\beta=0.012$,$\sigma_k=1.0$,$\sigma_\varepsilon=1.3$,$C_\mu=0.0845$, $C_{1,\varepsilon}=1.42$, $C_{2,\varepsilon}=1.68$
		ε	$\mu+\frac{\mu_t}{\sigma_\varepsilon}$	$C_{1\varepsilon}G_k\frac{\varepsilon}{k}-C_{2\varepsilon}\rho\frac{\varepsilon^2}{k}-R_\varepsilon$	
Realizable k-ε		k	$\mu+\frac{\mu_t}{\sigma_k}$	$G_k+G_b-\rho\varepsilon$	$\mu_t=\rho C_\mu\frac{k^2}{\varepsilon}$,$G_k=\mu_t S^2$, $S=\sqrt{2S_{ij}S_{ij}}$, $G_b=\beta g_i\frac{\partial\mu_t}{\partial\sigma_{T,t}}\frac{\partial\bar{T}}{\partial x_i}$, $\eta=Sk/\varepsilon$, $C_1=max\left[0.43,\frac{\eta}{\eta+5}\right]$, $C_2=1.9$, $C_{1,\varepsilon}=1.44$, $C_\mu=\frac{1}{A_0+A_s(kU*/\varepsilon)}$,$U*\equiv\sqrt{S_{ij}S_{ij}+\tilde{\Omega}_{ij}\tilde{\Omega}_{ij}}$, $\sigma_k=1.0$, $\sigma_\varepsilon=1.2$,
		ε	$\mu+\frac{\mu_t}{\sigma_\varepsilon}$	$\rho C_1 S_\varepsilon-\rho C_2\frac{\varepsilon^2}{k+\sqrt{\upsilon\varepsilon}}$	
SST k-ω		k	$\mu+\frac{\mu_t}{\sigma_k}$	G_k-Y_k	$\mu_t=\frac{\rho k}{\omega}\frac{1}{max[(1/\alpha*),SF_2/a_1\omega]}$, $\sigma_k=\frac{1}{\frac{F_1}{\sigma_{k,1}}+\frac{(1-F_1)}{\sigma_{k,2}}}$, $\sigma_\omega=\frac{1}{\frac{F_1}{\sigma_{\omega,1}}+\frac{(1-F_1)}{\sigma_{\omega,2}}}$, $G_k=\mu_t S^2$, $G_\omega=\frac{\alpha}{\nu_t}\tilde{G}_k$, $\tilde{G}_k=min(G_k,10\rho\beta^*k\omega)$, $Y_k=\rho\beta^*k\omega$, $Y_\omega=\rho\beta\omega^2$, $\sigma_{k,1}=1.176$, $\sigma_{\omega,1}=2.0$, $\sigma_{k,2}=1.0$, $\sigma_{\omega,2}=1.168$, $a_1=0.31$
		ω	$\mu+\frac{\mu_t}{\sigma_\omega}$	$G_\omega-Y_\omega$	

587